

The essence of long-range order in hybrid perovskites

Jonathan Lahnsteiner,¹ Ryosuke Jinnouchi,¹ and Menno Bokdam^{1,*}

¹University of Vienna, Faculty of Physics and Center for Computational Materials Sciences, Sensengasse 8/12, 1090 Vienna, Austria

(Dated: September 27, 2022)

The crystal structure of the MAPbI₃ hybrid perovskite forms an intricate electrostatic puzzle with different molecular ordering patterns at elevated temperatures. With Monte-Carlo simulations we show that model Hamiltonians based on the point-dipole approximation can, qualitatively, capture the long-range order observed in the low-temperature orthorhombic phase and describe the order-disorder transition. By comparing the coupling energetics of Methylammonium cations obtained by density functional theory calculations in cubic MA_xCs_{1-x}PbI₃ test systems, we show that the point-dipole approximation holds. The dipole-dipole (d-d) coupling splits the degeneracy of the states imposed by short-ranged interactions that are added to mimic the PbI framework interaction. To improve the accuracy of the d-d coupling, an Ewald summation is applied and a distance dependent model screening function is introduced. Our analysis indicates that essence of the long-range order can be reduced to effective interactions within a 6 Å radius. Such interactions are complex to model by hand, but can be captured by a recently presented machine-learning force field¹.

I. INTRODUCTION

The finite temperature structure of the promising Methylammonium-Lead Iodide (MAPbI₃) hybrid perovskite solar cell material is characterized by a vast number of accessible macro-states related to the orientational degree of freedom of the Methylammonium (MA) molecule. Above ~ 333 K, a cubic crystal structure is formed by PbI₆ octahedra enclosing MA molecules. Below ~ 150 K, an orthorhombic lattice is formed, with molecules in a long-range ordered pattern. The MA⁺Pb²⁺I₃⁻ system is held together by a mixture of covalent and ionic bonds, whereby the MA molecule is chemically decoupled from the PbI framework. Weak (hydrogen, van der Waals) bonds link the MA molecule to the framework³⁻⁶ and the intrinsic dipole moment ($|\mathbf{p}|$) of the molecules couples them, even more weakly, to each other⁷. There is a large spread in the reported MA preferred orientations as well as in their rotation barriers (10-100 meV), see Ref.⁸ and references therein. On one thing all seem to agree, at room temperature and above the molecules show entropic disorder⁹ in their orientations. It is important to understand the ordering pattern (or lack thereof) of the MA molecules, since the orientation of the molecules are tied to often interlinked inter-

actions (screening, charge localization, polarons, Rashba) which affect electronic device properties^{7,10-18}. Previous first-principles based molecular dynamics (FPMD) calculations have indicated that a soft long-range ordering pattern between neighboring MA molecules remains at room temperature^{8,19}. This order is a remnant of the highly ordered molecular pattern in the low-temperature orthorhombic phase. This order has been well resolved in experiment and is sketched in Figure 1. This pattern also shows the lowest energy in DFT calculations^{4,19-23}. However, the length and time scales required to model the finite temperature structure occurring in real devices exclude a straightforward application of FPMD methods. Therefore effective model Hamiltonians that describe the potential energy surface of MA molecules on a lattice could be of great help in understanding the local structure at defects²⁴ and domain boundaries²⁵. The presence of the reorienting molecules makes it difficult to apply models used for other perovskites, like BaTiO₃²⁶. Therefore point-dipole (pd) based model Hamiltonians^{25,27-34}, a rigid rotor cluster expansion³⁵ and classical force fields^{36,37} have been designed. Often the pd-models have been constructed in such a way that the heat capacity as function of temperature and/or phase transitions resemble experimental data. In some cases the coupling energies of certain inter-molecular ordering patterns have been fitted to DFT energies calculated for (relaxed) surrogates of the structure at different temperatures obtained from the experiment³⁸⁻⁴³. The local microscopic structure is in most experiments only observed on a time and space average. These surrogates show dynamic instabilities that manifest themselves as imaginary phonon frequencies in FP calculations^{44,45}. This indicates that the higher temperature crystal phases are possibly entropically stabilized. When many different micro-states of the molecular orientation are accessible, the related gain in entropy can shift the Gibbs free energy of the system such that the tetragonal and cubic phases are stabilized under certain temperature and

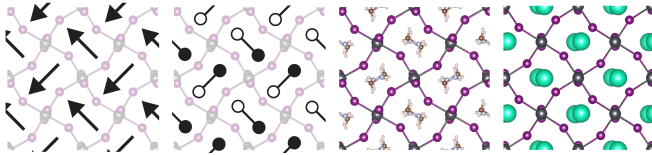


FIG. 1. The low temperature orthorhombic structure of MAPbI₃ in the i) point-dipole model, ii) monopole model and iii) the machine-learning force field. Arrows indicate the point-dipoles $\hat{\mathbf{p}}$ and their monopole based equivalents are shown by the black&white circles. The low temperature orthorhombic structure of CsPbI₃² is shown in the last figure.

pressure conditions.

In this work, we compare the inter-molecular structure at elevated temperature described by three recently published point-dipole based models^{27,28,31,32} to a highly accurate machine learned force field (MLFF)¹. The MLFF has the advantage that it learns *on-the-fly* during FPMD and generates ensembles that are practically indistinguishable from FPMD at much lower computational cost. By Monte Carlo calculations we study the change of this ordering pattern for the different models when the temperature is slowly raised. We show that the models have completely different ground states as well as excited states. One of the models³¹ is able to show qualitatively similar behavior as the MLFF. With DFT calculations on cubic MA_xCs_{1-x}PbI₃ supercells we demonstrate that the point-dipole approximation of the MA molecule has a limited accuracy. By summing the dipole-dipole (d-d) electrostatic energy in reciprocal space by means of an Ewald sum and by introducing a distance dependent model screening function we improve the accuracy. We show that the d-d coupling is important because it splits the degeneracy of the states imposed by short-range interactions. These interactions are the dominant energetic terms as can already be inferred from the experimentally observed long-range order in the low-temperature structure (Fig. 1). The molecules do not display a "striped" configuration (anti-ferroelectric aligned columns of head-to-tail dipoles), but rather close to orthogonal orientations. Our analysis indicates that essence of this long-range order can be reduced to effective interactions within a 6 Å radius.

This paper is organized as follows. In Section II we introduce the different model Hamiltonians, followed by a description of the applied Monte Carlo strategy and computational details in Section III. The results are presented in Section IV and, for readability, split into several subsections. The paper is closed with a discussion in Section V and its conclusions are summarized in Section VI.

II. MODEL HAMILTONIANS

Several model Hamiltonians describing the interactions of MA dipoles on a grid have been proposed in the last five years^{25,27-34}. In these models an effective Hamiltonian splits the total interaction energy of all N molecules in the cell in a short-range framework-dipole interaction and a long-range dipole-dipole interaction: $H = H_{\text{sr}} + H_{\text{lr}}$. The interaction terms are often very similar in these models, therefore we will limit the analysis to three representatives. For the models here considered (hereafter referred to as, I^{27,28}, II³², III³¹), the long-range part (H_{lr}) is based on the electrostatic interaction energy of two point-dipoles

$$U(\mathbf{p}_i, \mathbf{p}_j, \mathbf{n}_{ij}) = \frac{|\mathbf{p}|^2}{4\pi\epsilon_0\epsilon_r} \frac{1}{r_{ij}^3} (\hat{\mathbf{p}}_i \hat{\mathbf{p}}_j - 3(\hat{\mathbf{p}}_i \cdot \hat{\mathbf{n}}_{ij})(\hat{\mathbf{p}}_j \cdot \hat{\mathbf{n}}_{ij})), \quad (1)$$

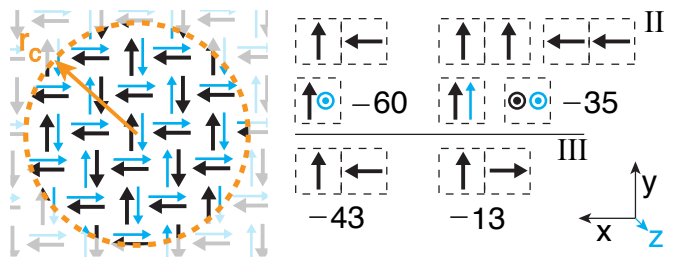


FIG. 2. Point-dipole model on a cubic lattice with interaction radius (r_c). The pair-modes assigned in models II and III together with the corresponding penalty potentials $g(\hat{\mathbf{p}}_i, \hat{\mathbf{p}}_j)$ (in meV) are sketched on the right. The lower lying layer, into the paper z-direction, is colored in blue.

where $\hat{\mathbf{p}}_i$ and $\hat{\mathbf{p}}_j$ denote unit dipole vectors at different lattice sites. The distance between the dipoles is given by $r_{ij} = |\mathbf{n}_{ij}|$ and $\hat{\mathbf{n}}_{ij} = \mathbf{n}_{ij}/|\mathbf{n}_{ij}|$ is the unit pointing vector. The total long-range energy is then calculated by a sum over all neighbors within the interaction radius (r_c) and then summed over all lattice sites,

$$H_{\text{lr}} = \frac{1}{2} \sum_{i=1}^N \sum_{j \in r_c} U(\mathbf{p}_i, \mathbf{p}_j, \mathbf{n}_{ij}). \quad (2)$$

All dipoles have the same dipole moment $|\mathbf{p}|$, but the relative permittivity ϵ_r and the long-range cutoff ($r_c^{\text{I}} = 3a$, $r_c^{\text{II}} = 2a$) depend on the model. In model II the Ewald summation technique is used to compute H_{lr} . In the three models the prefactor in Eq. (1) is treated as an effective coupling constant and an optimally tuned value is used. These values can be compared by ϵ_r when we define the dipole moment of the MA molecule to 2.29 D²⁷. This results in $\epsilon_r^{\text{I}} = 1$, $\epsilon_r^{\text{II}} = 0.73$, $\epsilon_r^{\text{III}} = 1.5$.

The short-range interaction (H_{sr}) is differently modeled in models I, II and III. In model I, it is described by a linear pair potential,

$$H_{\text{sr}}^{\text{I}} = -K \frac{1}{2} \sum_{i=1}^N \sum_{j \in n.n.} \hat{\mathbf{p}}_i \cdot \hat{\mathbf{p}}_j, \quad (3)$$

where the first sum runs over all lattice sites and the second sum over the nearest neighbors (n.n.). The parameter $K = 25$ meV approximates the strain on the framework and favors the parallel arrangement of dipoles. Both models II and III use a penalty potential of the form,

$$H_{\text{sr}}^{\text{II/III}} = \frac{1}{2} \sum_{i=1}^N \sum_{j \in n.n.} g(\hat{\mathbf{p}}_i, \hat{\mathbf{p}}_j). \quad (4)$$

The strength of the penalty depends on the relative orientations of n.n. molecules as sketched in Figure 2. In model II, two interaction modes are described: the pair of molecules lie "flat" in a common plane ($(\hat{\mathbf{p}}_i \times \hat{\mathbf{p}}_j) \cdot \hat{\mathbf{n}}_{ij} = 0$) and (i) they are orthogonal and one of them points to

the neighbor in the pair, then $g(\uparrow, \leftarrow) = -60$ meV, or (ii) they are pointing in the same direction, then $g(\uparrow, \uparrow) = -35$ meV. For all other n.n. configurations that can occur, $g = 0$ meV. Model III, also describes only two pair modes, but these modes are more restricted: the pair of molecules lie orthogonal to each other in the xy -plane and one of them points (i) to the neighbor in the pair, then $g(\uparrow, \leftarrow) = -43$ meV, or (ii) away from the neighbor in the pair, then $g(\uparrow, \rightarrow) = -13$ meV. As before, for all other nearest neighbor configurations that can occur, $g = 0$ meV. We note that the explicit preference for the xy -plane breaks the cubic symmetry of the Hamiltonian. In reality upon cooling from cubic to the orthorhombic phase, the molecules can condense in any of the cubic planes.

In regard to the short-range interaction of Eq. (4) we would like to mention the thorough work of Li *et.al.*, who have systematically analyzed the "pair-mode" concept based on $4 \times 4 \times 4$ supercell DFT calculations³³. The pair-modes used in models II and III also appear in their study as low energy configurations.

III. COMPUTATIONAL DETAILS

Monte-Carlo method. All the model Hamiltonians are evaluated by Monte-Carlo methods based on the Metropolis-Rosenbluth algorithm⁴⁶. $16 \times 16 \times 16$ dipole grids based on a cubic lattice ($a = 6.3$ Å) using periodic boundaries conditions were simulated. The starting configuration is a minimal representation of the molecular order in the experimental low-temperature (orthorhombic) structure. It solely consists out of x and y axes orientated molecules as sketched in Fig. 1 and the next plane in z direction has the same orientations anti-ferro-electrically aligned. Starting from the same configuration we calculate 20 Markov chains in parallel. The random number generator is initialized differently for every core to obtain different trajectories. Every chain equilibrates the system at the desired temperature by calculating $4 \cdot 10^6$ MC steps and then produces 25 equidistant samples spaced by $10 \cdot 16^3$ MC steps. Hereafter the temperature is increased by 10 K and the system is equilibrated again. This procedure is 60 times repeated, thereby raising the temperature from 0 to 600 K. Statistical averages are calculated over the chains. This setup has been carefully tested and shows converged order parameters.

Model I maps the orientational freedom of the dipoles on 26 discrete cubic orientations: $6 \times [1, 0, 0]$ (axes), $12 \times [1, 1, 0]$ (face diagonal) and $8 \times [1, 1, 1]$ (room diagonal). To avoid a bias for an orientation, we have weighted the chances in the Monte Carlo steps accordingly. Models II and III are more restrictive and allow only for the six cubic axes directions. The cutoff-radii for the long-range interaction were set as in the respective publications, ie. $r_c^I = 3a$, $r_c^{III} = 2a$. For model II the Ewald technique as presented in Ref. 47 is used instead of the real space summation.

Density Functional Theory. For the first-principles calculations we use a plane-wave basis and the projector augmented wave (PAW) method⁴⁸ as implemented in the VASP code^{49–51}. For the DFT calculations on the $MA_xCs_{1-x}PbI_3$ test systems, the PBE (Perdew-Burke-Ernzerhof)⁵² functional and standard VASP pseudo-potentials are used with a 400 eV energy cut-off for the plane-wave basis. Gaussian smearing with $\sigma = 0.05$ eV is used to broaden the one-electron levels. The Brillouin zone is sampled by a $2 \times 2 \times 2$ Γ -centered Monkhorst-Pack grid. The Kohn-Sham orbitals are updated in the self-consistency cycle until an energy convergence of 10^{-6} eV is obtained. $2 \times 2 \times 2$ $CsPbI_3$ super cells were constructed out of cubic unit cells with lattice constant $a = 6.3$ Å. On two sites, Cs atoms are replaced by Methylammonium (CH_3NH_3) molecules. All positions are kept fixed at their high symmetry cubic sites. The central molecule is rigidly rotated in spherical coordinates around the center of the C-N bond. No ionic relaxation was performed in these test systems.

Molecular Dynamics. The machine-learned force field (MLFF) of $MAPbI_3$ as presented in Ref.¹ is used to generate MD trajectories. The MLFF was trained *on-the-fly* during FPMD calculations with the SCAN (Strongly Constrained Appropriately Normed)⁵³ exchange-correlation functional, as its relative total energies agree well with many-body perturbation theory calculations in random phase approximation⁵⁴. The MLFF approach has the advantage that it speeds up the MD by three orders of magnitude, while retaining near FP accuracy. Note that the finite temperature structure of $MAPbI_3$ obtained with the MLFF is in excellent agreement with traditional FPMD^{8,19}. Further computational details are presented in Ref.¹. Here we have calculated a 600 ps long trajectory for a $4 \times 4 \times 4$ supercell (768 atoms) in the NPT ensemble. The temperature was linearly increased from 100 to 400 K using a Langevin thermostat⁵⁵. Since the heating trajectory shows signs of hysteresis, we have calculated the averaged molecular order parameter on constant temperature MDs. In these calculations snapshots of the heating run were equilibrated for 0.2–1.2 ns, depending the crystal phase and temperature.

IV. RESULTS

The results are presented in four subsections. We start by introducing an order parameter for the molecules, followed by a comparison of models I-III with MD. Hereafter we study the working of the short-range and long-range interactions separately.

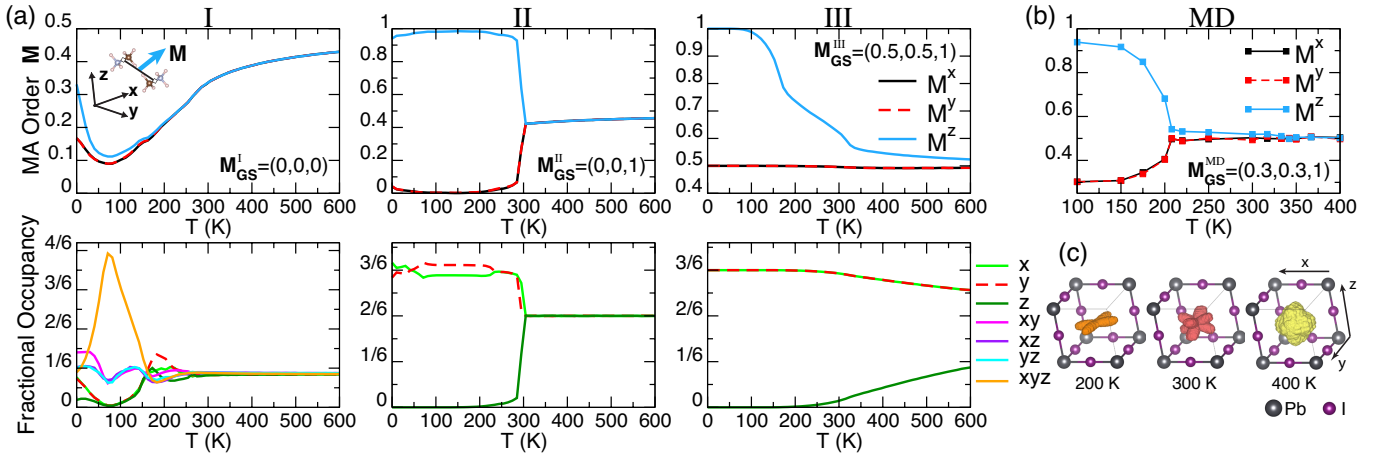


FIG. 3. (a) Molecular order parameter (\mathbf{M}) and fractional occupancy of orientational states as function of temperature for models I-III. Systems (I-III) are initialized at 0 K in state $\mathbf{M}_{init} = (0.5, 0.5, 1)$ and the true ground state ordering is indicated by \mathbf{M}_{GS} . (b) The squares show the average order \mathbf{M} obtained in constant temperature molecular dynamics (MD). (c) Three-dimensional polar distribution of the molecular C-N axes at three different temperature regimes in the MD.

A. Molecular Order Parameter

In order to straightforwardly compare the ordering patterns of the MA molecules we calculate the molecular order parameter as briefly presented Ref.¹. We assume an integer cubic grid $\mathbf{q} = (i, j, k)$ of dimensions $N = 16 \times 16 \times 16$ that has on each site a unit vector $\hat{\mathbf{p}}_{\mathbf{q}}$ describing the orientation of the MA molecule. The order parameter, $\mathbf{M} = (M^x, M^y, M^z)$, is then defined as

$$M^\alpha = \frac{1}{N\pi} \sum_{\mathbf{q}} \arccos(\hat{\mathbf{p}}_{\mathbf{q}} \cdot \hat{\mathbf{p}}_{\mathbf{q}+\mathbf{n}^\alpha}), \quad (5)$$

where \mathbf{n}^α is the displacement vector to the neighboring site in the Cartesian direction α . Typical order parameters in the three different crystal phases are:

$$\begin{aligned} \mathbf{M}_{ortho} &= (0.3, 0.3, 1) \\ \mathbf{M}_{tetra} &= (0.5, 0.5, 0.53) \\ \mathbf{M}_{cub} &= (0.5, 0.5, 0.5). \end{aligned} \quad (6)$$

These values agree well with the experimental structures as long as the temperature is not too close to the phase transition temperature¹.

B. Molecular ordering at finite temperature

To compare the ordering patterns of the MA molecules imposed by the model Hamiltonians, we have calculated large finite temperature ensembles by slowly heating up the experimental low temperature molecular configuration as shown in Figure 1. The distributions for the model systems were obtained by Monte Carlo simulations on a large cubic dipole grid. In Figure 3(a) the change of the order parameter (\mathbf{M}) during heating is shown. For

comparison, the same analysis of well-equilibrated constant temperature MDs based on the MLFF is shown in Fig. 3(b). The initial structure for the models is described by $\mathbf{M}_{init} = (0.5, 0.5, 1)$ and for the MD by \mathbf{M}_{ortho} . \mathbf{M}_{init} is the closest equivalent of \mathbf{M}_{ortho} described with only axes orientations of the molecules. This structure is already broken down at 0 K by models I and II, because it is not the true ground state (GS). Model II switches directly to its GS, which is an anti-ferroelectric striped pattern, $\mathbf{M}_{GS}^{II} = (0, 0, 1)$. Model I exhibits a kinetic barrier from $\mathbf{M}_{init} \rightarrow \mathbf{M}_{GS}^I = (0, 0, 0)$ and reaches it only partially at 75 K. Its GS is the fully polarized state with molecules ordered along one of the *room diagonal* (xyz) orientations. Model III and the MD retain the initial ordering at low temperature and show a gradual transition to a cubic-like phase. The different behavior of model I does not come as a surprise, its Hamiltonian has cubic symmetry and has no short-range interaction that can stabilize "flat" molecular orientations in the xy , xz or yz planes. Models II and III do have such interactions, imposed by favoring certain pair configurations. In model II, these pairs are counted for independently in which plane they lie, therefore the observed symmetry breaking is imposed by the initial structure only. Above ~ 300 K the system abruptly switches to a cubic-like phase, indicating a first order phase transition. Compared to MD, model III shows the largest similarity, with two transitions at roughly 150 and 300 K. At these temperatures the calculated heat capacity shows peaks³¹. Interestingly, when turning off the long-range dipole-dipole interactions, model III breaks \mathbf{M}_{init} down to \mathbf{M}_{cub} at low temperature, even though the pair configurations only favor the xy -plane and can perfectly form the initial molecular order. We come back to this stabilizing effect in Section IV C.

The second row of Fig. 3(a) shows the fractional occupancy of each quantized molecular orientation. Model

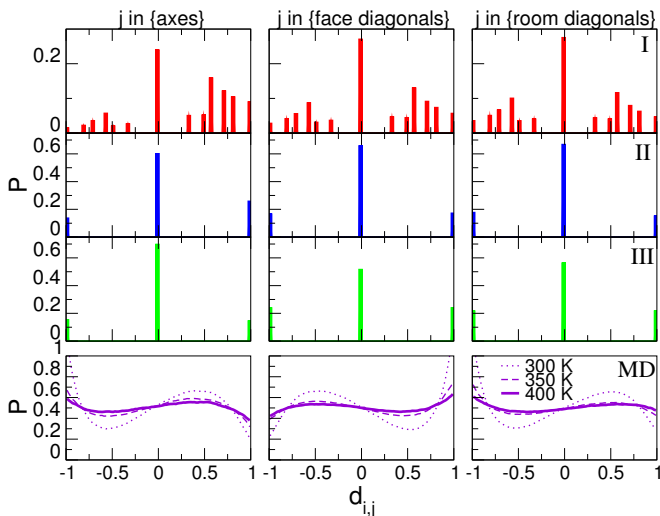


FIG. 4. Probability distributions of the relative molecular orientations ($d_{i,j} = \hat{\mathbf{p}}_i \cdot \hat{\mathbf{p}}_j$) in the first (axes), second (face diagonal) and third (room diagonal) nearest neighbor shells at 400 K. The MD distributions at 300 and 350 K are shown additionally.

I distinguishes 26 orientations, model II and III only 6 orientations and in the MD the molecules have the full rotational and translational degrees of freedom. At high temperature all orientations become equally occupied. Note here that there are eight *room diagonal* orientations (xyz), compared to four *face diagonals* (xy) and two *axes* (x) orientations, therefore these directions are weighted accordingly. To build a model that describes all three crystal phases by their typical molecular orientations, one minimally needs the axes basisset. The expected occupancy of the orientations would then be for orthorhombic: $(1/2, 1/2, 0)$, tetragonal $(1-\delta/2, 1-\delta/2, \delta)$ and cubic: $(1/3, 1/3, 1/3)$.

Model III can qualitatively reproduce the long-range order at low temperature and the transitions from this structure at higher temperature. However, this model cannot quantitatively reproduce the detailed molecular orientations observed in the MD simulations as well as in experiment. These orientations are illustrated in Figure 3(c) by the three-dimensional distributions of the molecular C-N axis calculated from MD. The three different temperatures show the typical orientations of the molecules in the three phases. These missing orientations are also important to describe the probability distributions of the relative molecular orientation ($d_{i,j} = \hat{\mathbf{p}}_i \cdot \hat{\mathbf{p}}_j$). In Figure 4 we see that the MLFF captures soft ordering that remains at room temperature and above, consistent with previous FPMD calculations¹⁹. In the first n.n. shell there is a broad peak at $d_{i,j} \approx 0.5$ and in the second at $d_{i,j} \approx -0.5$ and so on. When using the axes basisset, both relative orientations are mapped to $d_{i,j} = 0$. Expanding the basis with the face- and room-diagonal orientations would allow to reach a qualitative description for these relative orientations. To get real-

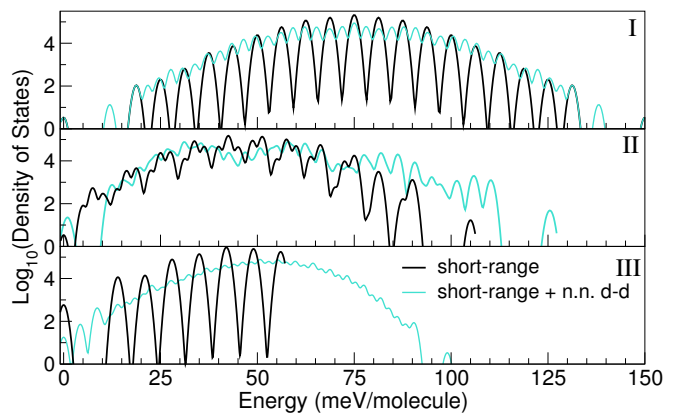


FIG. 5. Density of states (DOS) of models I-III on a $2 \times 2 \times 2$ cubic grid with only *axes* orientations including periodic boundaries with (turquoise) and without (black) n.n. dipole-dipole coupling. The ground state energy is set to zero. Gaussian smearing ($\sigma = 0.5$ meV) has been applied to broaden the δ -functions at each energy level. Note that the DOS is normalized ($\int DOS(E)dE = 6^8$) and its logarithm has been plotted.

istic microscopic structures one would have to include the dominant orientations as they occur in the MD. Figure 4 also indicates that all models show more structure at 400 K, whereas the MD distributions are almost flat.

C. Splitting of degenerate ground states by dipole-dipole interaction

Model III can capture the essence of the long-range order in the low temperature orthorhombic phase, although it fails to reproduce the more detailed molecular orientation. In order to clarify the origin of the long-range order, we analyze the short- and long-range interactions on the molecular orientations. As shown in Section II, the short-range interaction is the energetically dominant term in all model Hamiltonians I, II and III. It is built up of n.n. pair interactions and its ground state (GS) can be studied on a $2 \times 2 \times 2$ cubic grid with periodic

TABLE I. Bandwidth of the models (meV/molecule) as expressed by the standard deviation (σ) of the DOS and the energy difference between the ground- and highest state (ΔE). The multiplicity of the ground state (Ω) and the total number of different energy states (N_s) are shown in the last columns.

Model	σ	ΔE	Ω	N_s
Short-range I	12	150	6	21
Short-range I + n.n. dipole-dipole	15	150	6	95
Short-range II	12	105	6	41
Short-range II + n.n. dipole-dipole	17	126	6	257
Short-range III	9.3	56	1024	8
Short-range III + n.n. dipole-dipole	11	99	32	138
Short-range III + full dipole-dipole	-	-	8	-

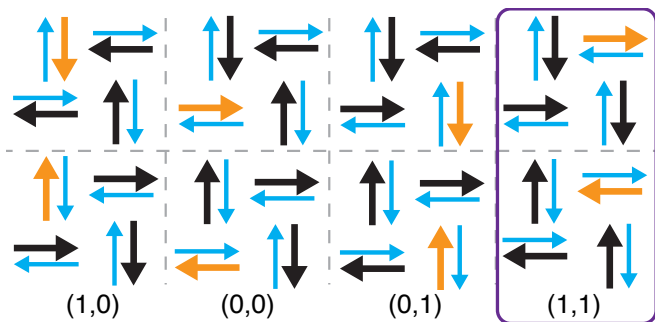


FIG. 6. Selection of 8 possible ordering patterns in the ground state of the short-range interaction (Eq. (4)) as parameterized in model III. The top xy plane is shown by the larger arrows and the underlying (anti-ferroelectric) layer is shown in blue. To highlight the relative changes one molecule is colored orange. The in-plane polarization vectors are indicated at the bottom. Inclusion of long-range d-d coupling makes the states marked with purple the ground state.

boundaries. Using only the 6 *axes* orientations we have calculated the total energies of all 6^8 possible ordering patterns. To illustrate the spread of these levels we have plotted the density of states (DOS) in Figure 5. We can roughly assess the influence of including the dipole-dipole coupling by calculating the n.n. interactions. In models II and III this increases the energy difference between the ground- and highest energy state (ΔE), whereas it is unaffected in model I. More importantly, many of the degenerate states are split, thereby raising the total number of different energy states (N_s). This also holds for the states occupied at room temperature (roughly those between 0-25 meV). In this small system with only n.n. interactions we can determine the GS exactly; model I shows a fully polarized state with multiplicity (Ω) of 6 and model II shows an anti-ferroelectric striped pattern also with $\Omega = 6$. Both GSs are different compared to the low temperature experimental ordering pattern of Fig 1. We have summarized the characteristics of the models in Table I and we will now discuss model III.

In Figure 6, eight out of a total of $\Omega = 1024$ possible ground states of *only* the short-range interaction (Eq. (4)) as parameterized in model III are sketched. The most in-plane polar states (highlighted in purple) that alternate between (1,1) and (-1,-1) polarized layers is the expected ordering. The inclusion of n.n. dipole-dipole coupling splits the degeneracy of the GS and brings its multiplicity down from $1024 \rightarrow 32$. It couples the layers in the z -direction to each other and enforces their anti-ferroelectric ordering. Still all states of Fig. 6 and further symmetry equivalents are possible ground states. If the cutoff radius of the d-d interaction is extended to include the next n.n. ($r_c = \sqrt{2}a$), the GS of Fig. 6 splits into three energy levels. Whereby the (1,1) state is the new GS with $\Omega = 8$, followed in energy by the (1,0) and (0,0) state. This means that d-d interaction in model III stabilizes the long-range ordering pattern to $\mathbf{M} = (0.5, 0.5, 1)$ and makes it the GS. This shows that an accurate de-

scription of the d-d coupling is important, because an underestimation enables a checkerboard pattern of the different orderings shown in Fig. 6 at low temperatures.

D. Accuracy of the long-range interaction

1. The $MA_xCs_{1-x}PbI_3$ test system

The point-dipole (pd) interaction plays an essential role in the stabilization of the correct long-range molecular order. However, the origin and validity of the selected parameters in model III are unclear. To test their accuracy, we have constructed $MA_xCs_{1-x}PbI_3$ test systems and examined the dipole-dipole interactions by DFT calculations. The systems are based on $2 \times 2 \times 2$ $CsPbI_3$ cubic supercells as shown in Figure 7. The central Cs atom is replaced by a MA molecule which is rotated manually. The DFT total energy (E) of the rotated configurations $\{0 \leq \phi < \pi/2, 0 \leq \theta < \pi\}$ is used to map out the short-range interaction energy $E_a(\phi, \theta)$. The obtained energy surface has a corrugation energy of ~ 80 meV with a room-diagonal orientation in the cubic PbI framework that is unfavored. Hereafter, a second Cs is replaced by a fixed MA molecule to probe the d-d coupling. As before, the central molecule is rotated and the DFT total energies are calculated. Depending on the position of the fixed molecule, see Figs. 7 (b) axes $\mathbf{n} = (\pm 1, 0, 0)$ and (c) room diagonal $\mathbf{n} = (\pm 1, \pm 1, \pm 1)$ neighbors, energy surfaces $E_b(\phi, \theta)$ and $E_c(\phi, \theta)$ are obtained, respectively. Assuming the short-range interaction is unaffected by the replacement of a neighboring Cs by MA, we can extract the long-range interaction energy by calculating

$$\Delta E_x = E_x - E_a - \langle E_x - E_a \rangle, \quad (7)$$

where $x = \{b, c\}$ and $\langle \cdot \rangle$ the average over $\{\theta, \phi\}$. The DFT long-range interaction energy obtained in test systems (b) and (c) are very well described by: $\Delta E_x = \alpha_x \cos \theta$, where $\alpha_b = -35$ meV and $\alpha_c = -10$ meV. In the point-dipole approximation these systems are described by $\Delta E_x^{\text{pd}} = H_{\text{lr}}$ with $N = 2$ and using periodic-boundaries. Summing the interaction in real space and cutting off the interactions beyond $r_c = \sqrt{3}a$, the following two energies are obtained

$$\Delta E_b^{\text{pd}} = -4 \frac{C}{a^3 \epsilon_r} \cos \theta, \quad \Delta E_c^{\text{pd}} = 0, \quad (8)$$

where $C = \frac{|\mathbf{p}|^2}{4\pi\epsilon_0}$ is the Coulomb constant. Setting $|\mathbf{p}|$ to 2.29 D fixes the energy scale to $C/a^3 \approx 13$ meV. As shown in Figure 7, the point-dipole model with the real space sum approximately reproduces the DFT results although this model fails to reproduce the cosine with amplitude of ± 10 meV observed in system (c).

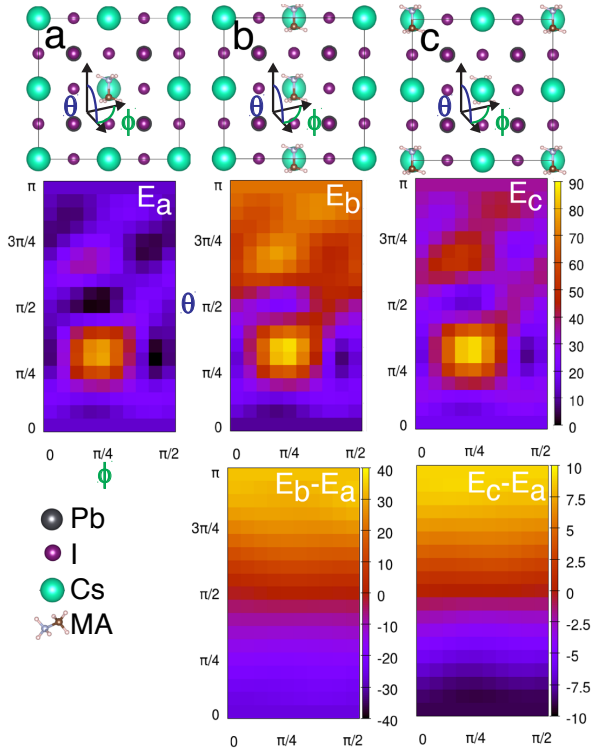


FIG. 7. *top*: The $\text{MA}_x\text{Cs}_{1-x}\text{PbI}_3$ test system in a $2 \times 2 \times 2$ cubic supercell. a) One MA molecule rotated by $\{\phi, \theta\}$. b) A fixed MA molecule at distance $r = a$ and direction $\hat{\mathbf{n}} = (0, 0, 1)$ replaces the Cs. c) Same as in b), but with $r = \sqrt{3}a$ and $\hat{\mathbf{n}} = 1/\sqrt{3}(1, 1, 1)$. *middle*: DFT total energy surfaces of systems a, b and c. *bottom*: DFT energy differences ($\Delta E_b, \Delta E_c$). The energy scale on all colorbars is in meV.

TABLE II. Parameters of the model dielectric function. Fitted screening length parameter ($\lambda_m = \lambda/a$) in \AA^{-1} and the "ion clamped" static dielectric constant (ϵ_∞) adapted from Ref. 56.

	λ/a	ϵ_∞		λ/a	ϵ_∞
MASnI ₃	1.05/6.23	9.18	MAPbBr ₃	1.13/5.91	5.15
FASnI ₃	1.05/6.33	8.06	FASnBr ₃	1.13/5.92	5.32
FAPbI ₃	1.05/6.35	7.10	FAPbCl ₃	1.17/5.71	4.27
MAPbI ₃	1.05/6.31	6.83	MAPbCl ₃	1.17/5.65	4.22
MASnBr ₃	1.13/5.86	5.89	FASnCl ₃	1.17/5.72	4.07
FAPbBr ₃	1.13/5.95	5.25	MASnCl ₃	1.17/5.67	4.05

2. Changes to the long-range interaction

Although the dipole-dipole interaction in the model III can roughly reproduce the DFT result, questions still remain since it is potentially a too simple formalism. In order to understand the physics behind this model, we further analyze the dipole-dipole interaction using three new electrostatic models.

First, considering the long-range nature of Eq. (1), the conditional convergence of Eq. (2) under the periodic boundaries that are imposed⁵⁷, H_{lr} should be calculated by an Ewald summation. Even though, models I and III

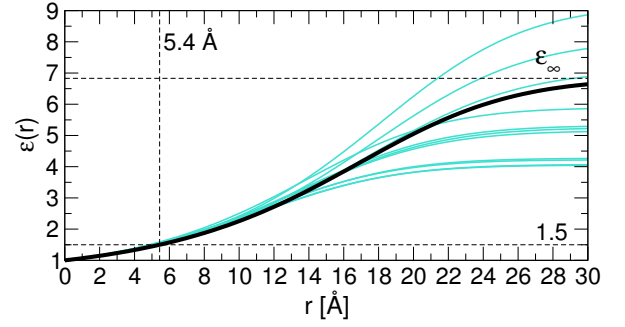


FIG. 8. Model dielectric function $\epsilon(r)$ for MAPbI_3 in the cubic phase based on the parameters of Table II. The range of screening strengths in the wider class of hybrid perovskites is plotted by the turquoise lines.

apply a real space sum. Here we apply the formulation of the Ewald sum as presented in Ref. 47. Note that the ($\mathbf{k} = 0$) term in the Ewald sum is omitted, implying that "conducting boundaries" are assumed⁵⁸.

Second, the microscopic electronic screening in this semiconductor can be more accurately described. Here, we apply the following distance dependent dielectric function

$$\epsilon_m^{-1}(r) = 1 - (1 - \epsilon_\infty^{-1}) \text{erf} \left(\frac{\lambda/a}{\sqrt{2\pi}} r \right), \quad (9)$$

where r is the distance and λ/a is the screening length. This is the real space version of the local model dielectric function fitted to the Many-Body Perturbation Theory (MBPT) calculations in the GW approximation as described in the supplementary materials of Ref. 56. The Fourier transform of $\epsilon^{-1}(\mathbf{k} + \mathbf{G}) \rightarrow \epsilon^{-1}(r)$ is described in Appendix A. Compared to one fixed effective dielectric constant (ϵ_r) this is a more realistic screening description with proper limits, $\epsilon(0) = 1$ and $\epsilon(\infty) = \epsilon_\infty$. We tabulate the parameters for a set of commonly studied hybrid perovskites in Table II and plot of $\epsilon(r)$ in Figure 8. We recall the ϵ_r values for the three models $\epsilon_r^{\text{I}} = 1$, $\epsilon_r^{\text{II}} = 0.73$, $\epsilon_r^{\text{III}} = 1.5$. Since the dominant contribution to the total dipole-dipole interaction energy comes from n.n. coupling, which occurs at distances of one lattice spacing ($\sim 6 \text{ \AA}$), setting $\epsilon_r < \epsilon_\infty$ as an effective screening parameter seems reasonable.

Third, the use of the point-dipole approximation can be circumvented by replacing the atoms with point charges, thereby creating interacting monopoles (mm). The system is sketched in Fig. 1 and is in total charge neutral. The same dipole moment as before is used to fix the charges: $q_{\text{C}} = 2.29 \cdot 0.20819434 \text{ e\AA} / 1.51 \text{ \AA} = 0.316e$, $q_{\text{N}} = -q_{\text{C}}$, $q_{\text{Pb}} = -2q_{\text{I}}$, $q_{\text{H}} = 0$ and $q_{\text{MA}} = q_{\text{Cs}} = -q_{\text{I}}$. A compensation charge q_{MA} is placed on the middle of the C-N bond. The Ewald sum is used to calculate the electrostatic energy of the monopole arrangements. Since the PbI framework and the center of mass of the molecule is fixed in this analysis, the charges q_{Pb} , q_{I} and q_{MA} only create a potential offset.

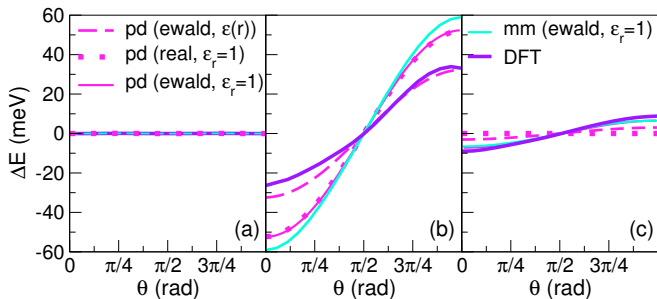


FIG. 9. Long-range interaction energy calculated in the point-dipole (pd) and monopole-monopole (mm) approximation using an Ewald and/or real space sum. Results are compared to the DFT data (ΔE_x) for the test systems (a), (b) and (c) in the respective figures.

In Figure 9, we have applied the three changes to the test systems (a-c). The most clear improvement is that by applying the Ewald sum (solid pink line) the cosine term is recovered for system (c). This term appears from the reciprocal space sum in the Ewald method. Note that the coupling to the second n.n. $\mathbf{n} = (\pm 1, \pm 1, 0)$ are correctly accounted for in the real-space sum. The mm-model (solid cyan line) shows almost the same result as the pd-model with the Ewald sum. This means that the distance between C and N is sufficiently small compared to the n.n. distance a . The cosine behavior of both systems (b) and (c) are captured by the pd-model with Ewald sum and $\varepsilon_r = 1$, but their amplitudes are not. In system (b) the coupling is overestimated, while it underestimates the coupling in system (c). Using the distance dependent dielectric function ($\varepsilon_m(r)$) the (b) system is quantitatively correct, but the coupling strength in system (c) is slightly underestimated.

Overall, the results indicate that the point-dipole approximation with the relatively short cutoff radius applied in model III is a qualitatively correct description of the long-range inter-molecule interaction. The minimum representation that enables the correct long-range ordered state at low-temperature is already obtained in the real-space sum with a short $r_c = \sqrt{2}a$ cut-off radius.

V. DISCUSSION

Model Hamiltonians of interacting point-dipoles on a cubic grid can assist in the qualitative understanding of the phase transitions in MAPbI₃. Such models can show similar order to disorder transitions and heat capacities as measured in experiment. With the Cs/MA-testsystem we removed what in most model studies of MAPbI₃ would be considered as the physical/chemical reasons for the short-range interactions. *Stress and strain* on the framework are removed because the framework is kept rigid under the MA rotation and the reference energy of system (a) is subtracted. We assume that the *hydrogen bonds* of the molecules with the framework are

only marginally affected by the rotation of a neighboring molecule and should therefore be taken away in this scheme. We have shown that in this system the point-dipole approximation with the short cutoff radius qualitatively captures the interaction between the molecules. The strength of the coupling is not in all geometries correct, but it does effectively split the degenerate ground state imposed by the short-range Hamiltonian. We extended the model with a physically-reasonable distance dependent screening effect and applied the Ewald summation technique, but the improvements are not substantial. The results indicate that the dipole-dipole interaction in this material can be represented by a short-ranged description.

The dipole-dipole coupling between the molecules is only an effective description of the electrostatics related to the ionic nature of the perovskite lattice. Without the MA cation, cubic PbI₃ is metallic in a DFT calculation. Introducing a MA or Cs turns it into a semiconductor. Each molecule donates one electron to the framework, which exactly fills up the (Pb and I states dominated) valence band. To lower the electrostatic energy, each MA⁺ points (with the nitrogen side) to a different PbI₃. The same mechanism also occurs in CsPbI₃, even though the Cs cation does not have an intrinsic dipole moment. As shown in the low temperature orthorhombic phases of Figure 1, similar off-center displacements for the Cs cations as for the center of masses of the MA molecules occur. And, in both perovskites the PbI octahedra show a clock-wise, anti-clockwise ordering. This results in stretched and squeezed cavities in which the molecules align, because of space filling, along the extended axes. The framework imposes the long-range order of the molecules, whereas the displaced centers of masses of the cations is the result of the ionic lattice.

In principle, such interactions can be described by a repulsive molecule-framework interaction and short-ranged monopole interactions as shown by our analyses. How-

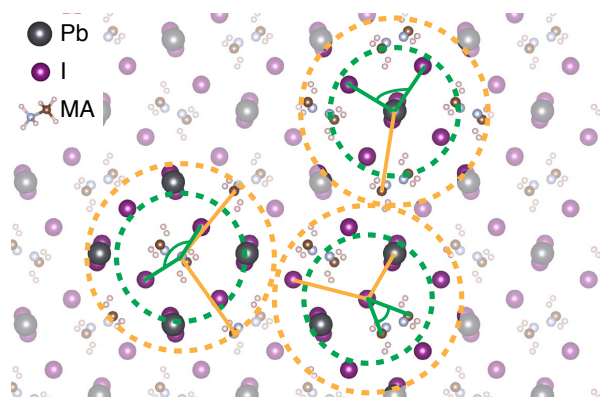


FIG. 10. Local chemical environment around a lead, nitrogen and iodine atom as recognized in the machine learning force field. Two-body radial and three-body angular descriptors with a cut-off of 6 Å and 4 Å are sketched in orange and green, respectively.

ever, improving on the present models is not an easy task. We have therefore applied a machine-learning force field approach which learns a force field *on-the-fly* during FPMD¹. This method shows ordering patterns, lattice constants and phase transition temperatures in very good agreement with experiments. The constraining effect of the PbI framework is automatically included, one of the difficult terms to model accurately. Furthermore, systems sizes of 10^4 - 10^5 atoms and nanosecond times scales become accessible for accurate modeling. The downside is that it does not produce a physically intuitive model, but that does not mean that its construction cannot give insight into the material. This force field is based on a purely short-range description as shown in Figure 10. Two-body radial and three-body angular descriptors with a cut-off of 6 Å and 4 Å, respectively, are used to represent the local chemical environment around each atom. The total energy is then defined as the sum of atomic energies assigned to each atom⁵⁹ by means of a similarity kernel. The fact that the MLFF works well means that model Hamiltonians based on two- and three-body descriptors would suffice. Long-range dipole-dipole coupling would in such a system not be necessary, which agrees with the minimum setup of the d-d interaction as deduced at the end of the previous Section. This leads to the conclusion that the essence of the long-range order of the molecules at low temperature lies in short-range interactions with a reach below 6 Å. The overlap of local atomic environments as sketched in Fig. 10 results in the propagation of long-ranged order.

VI. CONCLUSION

The atomic structure of the hybrid perovskite MAPbI₃ shows a rich palette of dynamics and crystal phases at elevated temperatures. Here, we compared the ordering pattern of Methylammonium molecules at finite temperatures imposed by three model Hamiltonians to accurate molecular dynamics simulations. We show that model III qualitatively describes the orthorhombic, tetragonal and cubic phase transitions based on simplified molecular ordering patterns. We have verified the applicability of the point-dipole approximation and have shown

that it splits the degenerated ground state imposed by the short-range Hamiltonian. We further examined the necessary range of the dipole-dipole interactions using more advanced electrostatic models with the distance dependent dielectric function and the Ewald summation technique. Dielectric screening parameters for several of the most studied hybrid perovskites have been presented. Although these new models enable a more quantitative description of the electrostatic interaction, the improvement is not substantial. This means that the essence of the long-range order of the molecules in the low temperature orthorhombic phase lies in the propagation of this order by short-range interactions between atoms that are no more than 6 Å apart. This explains the large similarity of the MAPbI₃ and CsPbI₃ crystal lattices, even though Cs does not have a dipole-moment.

In principle it is possible to improve the model Hamiltonian further by adopting a more elaborate description of the short-range interaction as well as inclusion of more refined molecular orientational degrees of freedom. However, its development and optimization *by-hand* is not tractable. In contrast, we demonstrated in this work that the machine-learning force field systematically constructs an accurate interaction model *on-the-fly* during first principles molecular dynamics. This method enables the automatic inclusion of the constraining effect of the PbI framework as well as the effective short-range electrostatics within a remarkable accuracy, thereby realizing very realistic ordering patterns of the molecules. The method can be extended to more complex systems with defects, surfaces and mixed halides or molecules. Therefore we believe that this new intelligent scheme can become a powerful tool to investigate structures and dynamics of complex materials at finite-temperature.

ACKNOWLEDGMENTS

Funding by the Austrian Science Fund (FWF): P 30316-N27 is gratefully acknowledged. Computations were performed on the Vienna Scientific Cluster VSC3. R.J. appreciates the financial support from Toyota Central R&D Labs., Inc. M.B. thanks Viktor Fournarakis and Lorenzo Papa for helpful discussions.

* menno.bokdam@univie.ac.at

¹ R. Jinnouchi, J. Lahnsteiner, F. Karsai, G. Kresse, and M. Bokdam, Phase transitions of hybrid perovskites simulated by machine-learning force fields trained on the fly with bayesian inference, *Phys. Rev. Lett.* (Accepted 14th of May 2019) (2019), [1903.09613](#).

² R. J. Sutton, M. R. Filip, A. A. Haghighirad, N. Sakai, B. Wenger, F. Giustino, and H. J. Snaith, Cubic or orthorhombic? revealing the crystal structure of metastable black-phase csppi3 by theory and experiment, *ACS Energy Lett.* **3**, 1787 (2018).

³ D. A. Egger and L. Kronik, Role of dispersive interactions in determining structural properties of organo-inorganic halide perovskites: Insights from first-principles calculations, *J. Phys. Chem. Lett.* **5**, 2728 (2014).

⁴ J.-H. Lee, N. C. Bristowe, P. D. Bristowe, and A. K. Cheetham, Role of hydrogen-bonding and its interplay with octahedral tilting in ch3nh3ppi3, *Chem. Commun.* **51**, 6434 (2015).

⁵ J. H. Lee, J.-H. Lee, E.-H. Kong, and H. M. Jang, The nature of hydrogen-bonding interaction in the prototypic hybrid halide perovskite, tetragonal ch3nh3ppi3, *Sci. Rep.*

- 6**, 21687 (2016).
- ⁶ J. Li and P. Rinke, Atomic structure of metal-halide perovskites from first principles: The chicken-and-egg paradox of the organic-inorganic interaction, *Phys. Rev. B* **94**, 045201 (2016).
 - ⁷ J. M. Frost, K. T. Butler, F. Brivio, C. H. Hendon, M. van Schilfgaarde, and A. Walsh, Atomistic origins of high-performance in hybrid halide perovskite solar cells, *Nano Lett.* **14**, 2584 (2014).
 - ⁸ J. Lahnsteiner, G. Kresse, J. Heinen, and M. Bokdam, Finite-temperature structure of the mapbi₃ perovskite: Comparing density functional approximations and force fields to experiment, *Phys. Rev. Mat.* **2**, 073604 (2018).
 - ⁹ A. Poglitsch and D. Weber, Dynamic disorder in methylammoniumtrihalogenoplumbates (ii) observed by millimeter-wave spectroscopy, *J. Chem. Phys.* **87**, 6373 (1987).
 - ¹⁰ J. Ma and L.-W. Wang, Nanoscale charge localization induced by random orientations of organic molecules in hybrid perovskite ch₃nh₃pbi₃, *Nano Lett.* **15**, 248 (2015).
 - ¹¹ F. Zheng, L. Z. Tan, S. Liu, and A. M. Rappe, Rashba spinorbit coupling enhanced carrier lifetime in ch₃nh₃pbi₃, *Nano Lett.* **15**, 7794 (2015).
 - ¹² C. Motta, F. El-Mellouhi, S. Kais, N. Tabet, F. Alharbi, and S. Sanvito, Revealing the role of organic cations in hybrid halide perovskite ch₃nh₃pbi₃, *Nature Comm.* **6**, 7026 (2015).
 - ¹³ T. Etienne, E. Mosconi, and F. De Angelis, Dynamical origin of the rashba effect in organohalide lead perovskites: A key to suppressed carrier recombination in perovskite solar cells?, *J. Phys. Chem. Lett.* **7**, 1638 (2016).
 - ¹⁴ A. J. Neukirch, W. Nie, J.-C. Blancon, K. Appavoo, H. Tsai, M. Y. Sfeir, C. Katan, L. Pedesseau, J. Even, J. J. Crochet, G. Gupta, A. D. Mohite, and S. Tretiak, Polaron stabilization by cooperative lattice distortion and cation rotations in hybrid perovskite materials, *Nano Lett.* **16**, 3809 (2016).
 - ¹⁵ J. Gong, M. Yang, X. Ma, R. D. Schaller, G. Liu, L. Kong, Y. Yang, M. C. Beard, M. Leslie, Y. Dai, B. Huang, K. Zhu, and T. Xu, Electronrotor interaction in organo-inorganic lead iodide perovskites discovered by isotope effects, *J. Phys. Chem. Lett.* **7**, 2879 (2016).
 - ¹⁶ S. Hu, H. Gao, Y. Qi, Y. Tao, Y. Li, J. R. Reimers, M. Bokdam, C. Franchini, D. Di Sante, A. Stroppa, and W. Ren, Dipole order in halide perovskites: Polarization and rashba band splittings, *J. Phys. Chem. C* **121**, 23045 (2017).
 - ¹⁷ B. Kang and K. Biswas, Preferential ch₃nh₃⁺ alignment and octahedral tilting affect charge localization in cubic phase ch₃nh₃pbi₃, *J. Phys. Chem. C* **121**, 8319 (2017).
 - ¹⁸ S. Govinda, B. P. Kore, M. Bokdam, P. Mahale, A. Kumar, S. Pal, B. Bhattacharyya, J. Lahnsteiner, G. Kresse, C. Franchini, A. Pandey, and D. D. Sarma, Behavior of methylammonium dipoles in mapbx₃ (x = br and i), *J. Phys. Chem. Lett.* **8**, 4113 (2017).
 - ¹⁹ J. Lahnsteiner, G. Kresse, A. Kumar, D. D. Sarma, C. Franchini, and M. Bokdam, Room-temperature dynamic correlation between methylammonium molecules in lead-iodine based perovskites: An *ab initio* molecular dynamics perspective, *Phys. Rev. B* **94**, 214114 (2016).
 - ²⁰ E. Menéndez-Proupin, P. Palacios, P. Wahnón, and J. C. Conesa, Self-consistent relativistic band structure of the CH₃NH₃PbI₃ perovskite, *Phys. Rev. B* **90**, 045207 (2014).
 - ²¹ M. R. Filip, G. E. Eperon, H. J. Snaith, and F. Giustino, Steric engineering of metal-halide perovskites with tunable optical band gaps, *Nature Comm.* **5**, 5757 (2014).
 - ²² M. R. Filip and F. Giustino, *gw* quasiparticle band gap of the hybrid organic-inorganic perovskite ch₃nh₃pbi₃: Effect of spin-orbit interaction, semicore electrons, and self-consistency, *Phys. Rev. B* **90**, 245145 (2014).
 - ²³ C. Quarti, E. Mosconi, and F. D. Angelis, Interplay of orientational order and electronic structure in methylammonium lead iodide: Implications for solar cell operation, *Chem. Mat.* **26**, 6557 (2014).
 - ²⁴ M. Šimėnas, J. Banyš, and E. E. Törnau, Screening of point defects in methylammonium lead halides: a monte carlo study, *J. Mater. Chem. C* **6**, 1487 (2018).
 - ²⁵ S. Ashhab, M. Carignano, and M. E. Madjet, Domain boundaries in luttinger-tisza ordered dipole lattices, *J. Appl. Phys.* **125**, 163103 (2019).
 - ²⁶ W. Zhong, D. Vanderbilt, and K. M. Rabe, First-principles theory of ferroelectric phase transitions for perovskites: The case of batio₃, *Phys. Rev. B* **52**, 6301 (1995).
 - ²⁷ J. M. Frost, K. T. Butler, and A. Walsh, Molecular ferroelectric contributions to anomalous hysteresis in hybrid perovskite solar cells, *APL Materials* **2**, 081506 (2014).
 - ²⁸ A. M. A. Leguy, J. M. Frost, A. P. McMahon, V. G. Sakai, W. Kockelmann, C. Law, X. Li, F. Foglia, A. Walsh, B. C. O'Regan, J. Nelson, J. T. Cabral, and P. R. F. Barnes, The dynamics of methylammonium ions in hybrid organic-inorganic perovskite solar cells, *Nature Comm.* **6**, 7124 (2015).
 - ²⁹ A. Pecchia, D. Gentilini, D. Rossi, M. Auf der Maur, and A. Di Carlo, Role of ferroelectric nanodomains in the transport properties of perovskite solar cells, *Nano Lett.* **16**, 988 (2016).
 - ³⁰ C. Motta, F. El-Mellouhi, and S. Sanvito, Exploring the cation dynamics in lead-bromide hybrid perovskites, *Phys. Rev. B* **93**, 235412 (2016).
 - ³¹ M. Šimėnas, S. Balčiūnas, M. Maczka, J. Banyš, and E. E. Törnau, Exploring the antipolar nature of methylammonium lead halides: A monte carlo and pyrocurrent study, *J. Phys. Chem. Lett.* **8**, 4906 (2017).
 - ³² L. Z. Tan, F. Zheng, and A. M. Rappe, Intermolecular interactions in hybrid perovskites understood from a combined density functional theory and effective hamiltonian approach, *ACS Energy Lett.* **2**, 937 (2017).
 - ³³ J. Li, J. Järvi, and P. Rinke, Multiscale model for disordered hybrid perovskites: The concept of organic cation pair modes, *Phys. Rev. B* **98**, 045201 (2018).
 - ³⁴ J. Järvi, J. Li, and P. Rinke, Multi-scale model for the structure of hybrid perovskites: analysis of charge migration in disordered mapbi₃ structures, *New J. Phys.* **20**, 103013 (2018).
 - ³⁵ J. C. Thomas, J. S. Bechtel, and A. Van der Ven, Hamiltonians and order parameters for crystals of orientable molecules, *Phys. Rev. B* **98**, 094105 (2018).
 - ³⁶ A. Mattoni, A. Filippetti, M. I. Saba, and P. Delugas, Methylammonium rotational dynamics in lead halide perovskite by classical molecular dynamics: The role of temperature, *J. Phys. Chem. C* **119**, 17421 (2015).
 - ³⁷ C. M. Handley and C. L. Freeman, A new potential for methylammonium lead iodide, *Phys. Chem. Chem. Phys.* **19**, 2313 (2017).
 - ³⁸ D. Weber, Ch₃nh₃pbx₃, ein pb(ii)-system mit kubischer perowskitstruktur / ch₃nh₃pbx₃, a pb(ii)-system with cubic perovskite structure, *Zeitschrift für Naturforschung B* **33**, 1443 (1978).
 - ³⁹ N. Onoda-Yamamuro, T. Matsuo, and H. Suga, Calori-

- metric and ir spectroscopic studies of phase transitions in methylammonium trihalogenoplumbates (ii), *J. Phys. Chem. Sol.* **51**, 1383 (1990).
- 40 T. Baikie, Y. Fang, J. M. Kadro, M. Schreyer, F. Wei, S. G. Mhaisalkar, M. Graetzel, and T. J. White, Synthesis and crystal chemistry of the hybrid perovskite (ch₃nh₃)pb₃ for solid-state sensitized solar cell applications, *J. Mater. Chem. A* **1**, 5628 (2013).
- 41 C. C. Stoumpos, C. D. Malliakas, and M. G. Kanatzidis, Semiconducting tin and lead iodide perovskites with organic cations: Phase transitions, high mobilities, and near-infrared photoluminescent properties, *Inorg. Chem.* **52**, 9019 (2013).
- 42 Y. Kawamura, H. Mashiyama, and K. Hasebe, Structural study on cubictetragonal transition of ch₃nh₃pb₃, *J. Phys. Soc. Jpn.* **71**, 1694 (2002).
- 43 P. Whitfield, N. Herron, W. E. Guise, K. Page, Y. Q. Cheng, I. Milas, and M. K. Crawford, Structures, phase transitions and tricritical behavior of the hybrid perovskite methyl ammonium lead iodide, *Sci. Rep.* **6**, 35685 (2016).
- 44 F. Brivio, J. M. Frost, J. M. Skelton, A. J. Jackson, O. J. Weber, M. T. Weller, A. R. Goñi, A. M. A. Leguy, P. R. F. Barnes, and A. Walsh, Lattice dynamics and vibrational spectra of the orthorhombic, tetragonal, and cubic phases of methylammonium lead iodide, *Phys. Rev. B* **92**, 144308 (2015).
- 45 A. M. A. Leguy, A. R. Goi, J. M. Frost, J. Skelton, F. Brivio, X. Rodriguez-Martinez, O. J. Weber, A. Palipurath, M. I. Alonso, M. Campoy-Quiles, M. T. Weller, J. Nelson, A. Walsh, and P. R. F. Barnes, Dynamic disorder, phonon lifetimes, and the assignment of modes to the vibrational spectra of methylammonium lead halide perovskites, *Phys. Chem. Chem. Phys.* **18**, 27051 (2016).
- 46 N. Metropolis, A. W. Rosenbluth, M. N. Rosenbluth, A. H. Teller, and E. Teller, Equation of state calculations by fast computing machines, *J. Chem. Phys.* **21**, 1087 (1953).
- 47 D. Frenkel and B. Smit, *Understanding Molecular Simulation (Second Edition)*, second edition ed., edited by D. Frenkel and B. Smit (Academic Press, San Diego, 2002) pp. 291 – 320.
- 48 P. E. Blöchl, Projector augmented-wave method, *Phys. Rev. B* **50**, 17953 (1994).
- 49 G. Kresse and J. Hafner, Ab-initio molecular-dynamics for liquid-metals, *Phys. Rev. B* **47**, 558 (1993).
- 50 G. Kresse and J. Furthmüller, Efficient iterative schemes for ab initio total-energy calculations using a plane-wave basis set, *Phys. Rev. B* **54**, 11169 (1996).
- 51 G. Kresse and D. Joubert, From ultrasoft pseudopotentials to the projector augmented-wave method, *Phys. Rev. B* **59**, 1758 (1999).
- 52 J. P. Perdew, K. Burke, and M. Ernzerhof, Generalized gradient approximation made simple, *Phys. Rev. Lett.* **77**, 3865 (1996).
- 53 J. Sun, A. Ruzsinszky, and J. P. Perdew, Strongly constrained and appropriately normed semilocal density functional, *Phys. Rev. Lett.* **115**, 036402 (2015).
- 54 M. Bokdam, J. Lahnsteiner, B. Ramberger, T. Schäfer, and G. Kresse, Assessing density functionals using many body theory for hybrid perovskites, *Phys. Rev. Lett.* **119**, 145501 (2017).
- 55 M. P. Allen and D. J. Tildesley, *Computer simulation of liquids* (Oxford university press, 1991).
- 56 M. Bokdam, T. Sander, A. Stroppa, S. Picozzi, D. D. Sarma, C. Franchini, and G. Kresse, Role of polar phonons in the photo excited state of metal halide perovskites, *Sci. Rep.* **6**, 28618 (2016).
- 57 G. Makov and M. C. Payne, Periodic boundary conditions in ab initio calculations, *Phys. Rev. B* **51**, 4014 (1995).
- 58 S. Chen and A. Bongiorno, Boundary conditions in periodic density functional calculations of insulating materials, *Phys. Rev. B* **83**, 165125 (2011).
- 59 A. P. Bartók, M. C. Payne, R. Kondor, and G. Csányi, Gaussian approximation potentials: The accuracy of quantum mechanics, without the electrons, *Phys. Rev. Lett.* **104**, 136403 (2010).

Appendix A: Real space dielectric function

The Coulomb potential in reciprocal space screened by the model dielectric function ϵ_m as presented in Ref. 56 is given by

$$V(\mathbf{k}) = \frac{4\pi}{\mathbf{k}^2} \epsilon_m^{-1}(|\mathbf{k}|) = \frac{4\pi}{\mathbf{k}^2} \left(1 - (1 - \epsilon_\infty^{-1}) e^{-\frac{\pi|\mathbf{k}|^2}{\lambda_m^2}} \right). \quad (\text{A1})$$

The screened Coulomb potential in real space is obtained by the Fourier transform of Eq. (A1),

$$V(\mathbf{r}) = \int_{-\infty}^{\infty} \left[\frac{4\pi}{\mathbf{k}^2} \left(1 - (1 - \epsilon_\infty^{-1}) e^{-\frac{\pi|\mathbf{k}|^2}{\lambda_m^2}} \right) \right] e^{i\mathbf{k}\mathbf{r}} d\mathbf{k}. \quad (\text{A2})$$

Switching to spherical coordinates and evaluating the integrals with respect to the spherical angles θ and φ gives,

$$V(r) = \frac{16\pi^2}{r} \int_0^\infty \left[\frac{1 - (1 - \epsilon_\infty^{-1}) e^{-\frac{\pi k^2}{\lambda_m^2}}}{k} \right] \sin(kr) dk. \quad (\text{A3})$$

Hereby, the problem reduces to solving the integrals

$$A(r) = \int_0^\infty \frac{\sin(kr)}{k} dk, \quad (\text{A4})$$

and

$$B(r) = \int_0^\infty \frac{\sin(kr) e^{-\frac{\pi k^2}{2\lambda_m^2}}}{k} dk. \quad (\text{A5})$$

To solve $A(r)$, a damping function $e^{-\beta k}$ is multiplied to the integrand. Note that in the limit of $\beta \rightarrow 0$ the original function is recovered. The derivative of this integral with respect to β is

$$\frac{dI(\beta, r)}{d\beta} = - \int_0^\infty \sin(kr) e^{-\beta k} dk = - \frac{r}{\beta^2 + r^2}. \quad (\text{A6})$$

The indefinite integral with respect to β results in the inverse tangent function $I(\beta, r) = -\arctan\left(\frac{\beta}{r}\right) + C$. By considering the limit $\beta \rightarrow \infty$,

$$I(\infty, r) = -\frac{\pi}{2} + C = \int_0^\infty \frac{\sin(kr)}{k} e^{-\infty k} dk = 0, \quad (\text{A7})$$

one can determine the integration constant $C = \pi/2$.
Thereby Eq. (A4) reduces to

$$A(r) = \frac{\pi}{2}. \quad (\text{A8})$$

To solve $B(r)$, one introduces $D = \frac{\pi}{2\lambda_m^2}$ and takes the derivative with respect to r ,

$$\frac{dB(r)}{dr} = \int_0^\infty e^{-Dk^2} \cos(kr) dk = \frac{1}{2} \int_{-\infty}^\infty e^{-Dk^2} e^{ikr} dk. \quad (\text{A9})$$

The integration over k simplifies to a 1-dimensional Fourier transform of a Gaussian function,

$$\frac{dB(r)}{dr} = \frac{\pi}{2D} e^{-\frac{r^2}{4D}}. \quad (\text{A10})$$

Integrating with respect to r results in

$$B(r) = \frac{\pi}{2} \operatorname{erf}\left(\frac{r\lambda_m}{\sqrt{2\pi}}\right). \quad (\text{A11})$$

Combining the Eqs. (A8) and (A11) with Eq. (A3) gives the real space screened Coulomb potential

$$V(r) = \frac{8\pi^3}{r} \varepsilon_m^{-1}(r), \quad (\text{A12})$$

where

$$\varepsilon_m^{-1}(r) = 1 - (1 - \varepsilon_\infty^{-1}) \operatorname{erf}\left(\frac{r\lambda_m}{\sqrt{2\pi}}\right). \quad (\text{A13})$$

is the inverse dielectric function in real space.